Programmable Coherent Linear Quantum Operations with High-Dimensional Optical Spatial Modes

Shikang Li,[1] Shan Zhang,[1] Xue Feng,[1,*] Stephen M. Barnett,[2] Wei Zhang,[1] Kaiyu Cui,[1] Fang Liu,[1] and Yidong Huang[1]

[1] *Department of Electronic Engineering, Tsinghua University, 100084 Beijing, China*

[2] *School of Physics and Astronomy, University of Glasgow, Glasgow, G12 8QQ, United Kingdom*

(Received 28 September 2019; revised 19 May 2020; accepted 16 June 2020; published 12 August 2020)

A simple and flexible scheme for high-dimensional linear quantum operations is demonstrated on optical discrete spatial modes in the transverse plane. Quantum-state tomography via symmetric informationally complete positive-operator-valued measures and quantum Fourier transformation are implemented with dimensionality of 15. The statistical fidelity of symmetric informationally complete positive-operator-valued measures and the fidelity of quantum-state tomography are approximately 0.97 and up to 0.853, respectively, while the matrix fidelity of quantum Fourier transformation is 0.85. We believe that our approach has the potential for further exploration of high-dimensional spatial entanglement provided by spontaneous parametric down-conversion in nonlinear crystals.

DOI: 10.1103/PhysRevApplied.14.024027

I. INTRODUCTION

Photonics provides an outstanding platform for exploring nonclassical computational resources [1] because entanglement can be conveniently generated through optical nonlinear effects [2–4], while linear manipulation protocols are available in multiple degrees of freedom [5–7]. Great efforts have been made to generate and manipulate high-dimensional entangled states, both for tests of quantum mechanics [8] and also for applications to quantum technology [9]. There is a push to increase the information encoded on a single photon [10] and achieve high-dimensional universal linear operation to extend the capacity of quantum processing as well as enhance the versatility of quantum computing and simulation [11].

High-dimensional quantum encoding has been demonstrated on photons in the optical path domain [12], frequency domain [4], temporal-mode domain [13,14], and transverse-spatial-mode domain [15–17]. For the first of these, Reck et al. [5] showed how arbitrary unitary operators could be realized using cascaded basic blocks consisting of phase modulators and couplers. With the scheme of Reck et al., programmable matrix operators and projectors with dimensionality from 6 to 26 [9,12,18,19] have been reported in the path domain. However, only a 6×6 arbitrary transformation matrix has been achieved, while other demonstrations are fixed or partially adjustable due to the growing arrangement complexity of phase shifters and directional couplers. In the frequency domain, quantum entanglement with Schmidt number up to 10 can be generated routinely through spontaneous four-wave mixing [4], but the dimensionality of the quantum operator or projector achieved is limited to 4 as ultrafast electro-optic modulation devices are required [4,7]. To exhibit substantial computational superiority, the dimensionality of fully tunable quantum operators has to be increased.

Transverse spatial modes provide abundant resources for quantum encoding and processing. Particularly, spatial-mode entanglement induced by spontaneous parametric down-conversion (SPDC) in nonlinear crystals [2,3,20–24] has been well investigated. Two-photon spatial entanglement with a high Schmidt number is potentially available with meticulously designed pump parameters [16,17,25]. However, the use of such quantum resources has been hindered by the lack of universal operation protocols. The scheme of Reck et al. works well with one-dimensional in-plane path encoding, but is not compatible with these spatial-mode-encoded states in the two-dimensional transverse plane. Quantum-operation protocols on orbital angular momentum, which can be considered as a specific basis of spatial modes, have been presented but only with limited dimensionality [6,26]. Thus, although high-dimensional universal quantum operations on spatial modes could boost the exploration of currently existing entanglement resources, an efficient approach remains to be demonstrated.

Here we tackle this issue by encoding the quantum information in the discrete coherent spatial (DCS) modes and demonstrating a distinctive method to implement arbitrary linear quantum operators. In contrast with the in-plane

*x-feng@tsinghua.edu.cn

path encoding, DCS modes can be flexibly and arbitrarily arranged in the two-dimensional transverse plane according to the optical beam propagation so that more-manageable manipulation can be achieved. Additionally, as our approach can be considered as the general form of path encoding and transverse mode encoding, the linear quantum operations on DCS modes will be compatible with both path-encoded qudits and spatial-mode-encoded qudits. Furthermore, it is possible to combine our approach with that in the frequency domain since they have independent degrees of freedom. In this work, various quantum operators are experimentally achieved with dimensionality up to 15×15, and we apply these to demonstrate symmetric informationally complete positive-operator-valued measures (SIC POVMs) and quantum Fourier transformation (QFT). This is the implementation of discrete arbitrary linear quantum operators with the highest reported dimensionality [6,7,9,12]. Because of the universality, precision, and controllability, our scheme makes possible high-dimensional demonstrations of nonclassical phenomena and quantum-information processing. This can be achieved by exploring fully multipath entanglement in the transverse plane, which can be provided by the whole spontaneous down-conversion cone [15] or integrated path-encoded photonic qudits with the help of three-dimensional waveguide coupling [27].

II. PRINCIPLE

Generally, with a set of well-defined orthogonal basis states, any linear operation can be expressed as $|\beta\rangle = T|\alpha\rangle$, in which T is a complex matrix and $|\alpha\rangle$ and $|\beta\rangle$ are initial and final state vectors in a complex vector space with dimensionality of N. In our previous work [28,29], the state vector of $|\alpha\rangle$ and $|\beta\rangle$ was encoded on a set of DCS modes $|\varphi_n\rangle = u(\mathbf{r} - \mathbf{R}_n)$. As indicated in Fig. 1(a), $\mathbf{R}_n$ is the transverse coordinate of the nth DCS mode, while $u(\mathbf{r} - \mathbf{R}_n)$ is considered a Gaussian function of $u(\mathbf{r} - \mathbf{R}_n) \propto \exp(-|\mathbf{r} - \mathbf{R}_n|^2/{w_0}^2)$ and the optical waist of w_0 is designed as sufficiently small compared with the transverse distance $|\mathbf{R}_n - \mathbf{R}_m|$ between two adjacent DCS modes to ensure orthogonality [29]. Hence, the state vector can be expressed as $|\alpha\rangle = \sum a_n|\varphi_n\rangle$.

For a given linear operator of T, one-to-N beam splitting and N-to-one beam recombining are required to achieve the columns and rows of a general transformation matrix. T should be decomposed as the Hadamard product of two matrices ($T_{mn} = A_{mn}B_{mn}$). The optimal decomposition to achieve maximum energy efficiency was discussed in our previous work [29]. With the obtained matrices of A and B, beam splitting and recombining can be implemented by two phase-only spatial light modulators (SLM1 and SLM2) combined with two $2f$ systems and a pinhole [Fig. 1(b)]. For a diffraction grating illuminated by an optical beam, the diffraction pattern on the Fourier plane of the diffraction grating is the convolution of the Fourier coefficients of the diffraction grating and the Fourier spectrum of the incident beam field according to diffraction theory [30]. Thus, the diffraction gratings on SLM1 and SLM2 are set according to the Fourier coefficients of A_{mn} and B_{mn}:

$$H_{1n}(\mathbf{r}) = \exp\left(i \arg\left\{\sum_{m=1}^{N} \mu_{mn} A_{mn} \exp[i\mathbf{k}_{mn} \cdot (\mathbf{r} - \mathbf{R}_n)]\right\}\right),$$
$$H_{2m}(\mathbf{r}) = \exp\left(i \arg\left\{\sum_{n=1}^{N} \nu_{mn} B_{mn} \exp[-i\mathbf{k}_{mn} \cdot (\mathbf{r} + \mathbf{R}_m]\right\}\right), \quad (1)$$

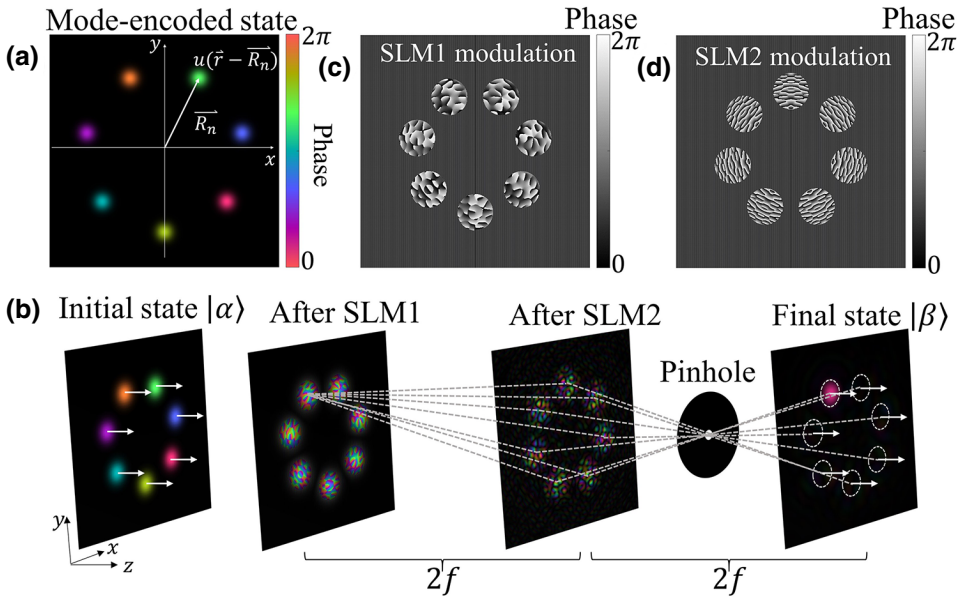

FIG. 1. (a) Definition of the discrete spatial modes. (b) Schematic setup for implementing linear quantum operators. A seven-dimensional QFT demonstration is shown as a concrete example. Simulated field evolution after each SLM is presented. Phase-modulation pattern implemented on SLM1 (c) and SLM2 (d) for beam splitting and recombining, respectively.

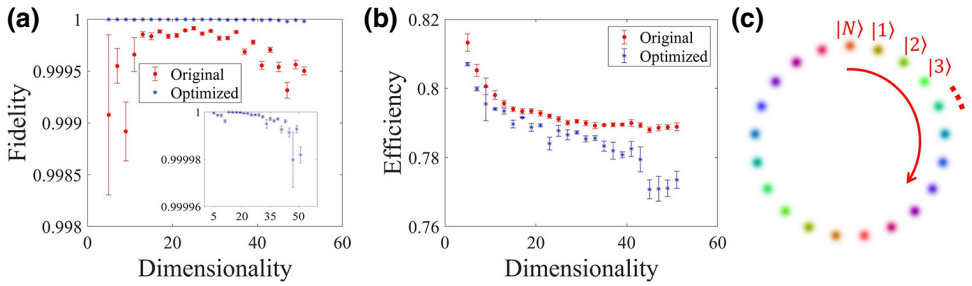

FIG. 2. Simulated fidelity (a) and efficiency (b) for one-to-N beam splitting. (c) The transverse coordinates of the spatial modes used are arranged on a circle.

where $\mathbf{k}_{mn}$ is the transverse wave vector expressed as $\mathbf{k}_{mn} = k(\mathbf{R}_n - \mathbf{R}_m)/2f$. Two sets of optimization coefficients, $\{\mu_{mn}\}$ and $\{\nu_{mn}\}$, are introduced to achieve the desired beam-splitting and beam-recombining ratio. The detailed modulation functions on SLMs are included in Appendix A. As a concrete example, the diffraction gratings for seven-dimensional QFT are displayed in Figs. 1(c) and 1(d).

We choose the same optimization algorithm as used in Ref. [31]. The fidelity between the target and the implemented matrix (A or B vs A_{exp} or B_{exp}) normalized by energy [32] is the optimization target:

$$F(A_{\text{exp}}, A) = \left| \frac{\text{Tr}(A^{\dagger} A_{\text{exp}})}{\sqrt{\text{Tr}(A_{\text{exp}}^{\dagger} A_{\text{exp}}) \times \text{Tr}(A^{\dagger} A)}} \right|^2 . \quad (2)$$

In Fig. 2, Huygens-Fresnel simulation results for beam splitting of dimensionality up to 51 are summarized. Each data point is the statistical combination of 20 random complex target matrices. The data labeled as "original" correspond to $\{\mu_{mn}\} \equiv 1$ without any optimization, while near-ideal fidelities can be achieved with a small efficiency penalty (less than 2%) after optimization. We believe that the imperfection is caused by a calculation error arising from iteration tolerance. The efficiency is calculated from $E(A_{\text{exp}}, A) = \text{Tr}(A_{\text{exp}}^{\dagger} A_{\text{exp}})/\text{Tr}(A^{\dagger} A)$. Similar simulation results are obtained with N-to-one beam recombining. The overall fidelity considering both beam splitting and beam recombining is approximately the square value of the fidelities plotted in Fig. 2. As shown in Fig. 2(c), the transverse coordinates of our proposed discrete spatial modes are arranged on a circle during these simulations to mimic the spatially sampled type-I SPDC cone.

III. RESULTS

Experiments are performed to verify and evaluate our scheme. Figure 3 illustrates the experimental setup, in which a heralded single-photon source and time-correlated single-photon counting (TCSPC) are used. A pulsed laser (Alnair PFL200) with a central wavelength of approximately 1552 nm serves as a degenerate pump to generate spontaneous four-wave mixing in a dispersion-shifted fiber [33]. The dispersion-shifted fiber is cooled to 77 K with liquid nitrogen to reduce the Raman-scattering noise. The time-correlated signal and idler photons are filtered out by dense-wavelength-division-multiplexing filters. The idler photons (1555.7 nm) are directly collected by an (In,Ga)As single-photon detector (IDQ220), which heralds the detection of a signal photon (1549.3 nm) after linear operation. The signal photons are collimated to a free-space Gaussian mode expressed as $|\varphi_0\rangle$ under DCS-mode basis $|\varphi\rangle\langle\varphi|$. A beam splitter noted as $|\alpha\rangle\langle\varphi_0|$ is programmed on an additional spatial light modulator (Holoeye Pluto) labeled "SLM0" to generate the initial qudit state $|\alpha\rangle = \sum a_n |\varphi_n\rangle$. The target operation $|\beta\rangle = T|\alpha\rangle$ is performed by SLM1 and SLM2 (operating in reflection mode). The projection values of the final state in the DCS-mode basis after the quantum operation, $|\langle\varphi_n|\beta\rangle|^2$, are detected by a single-photon avalanche detector with a monomode fiber coupler one by one. A different spatial distribution of DCS modes (inset in Fig. 3) from that used in the simulation [Fig. 2(c)] is chosen to fully utilize the spatial area of the SLMs and show the flexibility of our scheme. The spatial distribution of DCS modes can be properly designed according to the applied single-photon source or entanglement source. Particularly, SLM0 could be replaced by a SPDC source for a future biphoton-entanglement experiment, and the spatial sampling of the SPDC cone as well as beam splitting could be done simultaneously by SLM1.

Quantum-state tomography (QST) provides a full description of the quantum state [34]. Firstly, 15-dimensional QST is performed to present the ability of arbitrary-coherent-matrix operation with our proposal. In experiments, SIC POVMs are used. A SIC-POVM basis $|\Psi_{jk}\rangle\langle\Psi_{jk}|$ can be generated by applying N^2 displacement operators [35] on a fiducial vector $|f\rangle$ [36]:

$$|\Psi_{jk}\rangle = \exp\left(\frac{2jk\pi i}{N}\right) \sum_{m=0}^{N-1} |\text{mod}(k+m, N)\rangle\langle m|f\rangle. \quad (3)$$

QST is performed with a compressed-sensing method [37], with use of 100 randomly selected SIC POVMs from the 225 distinct elements. Figure 4 presents two sets of experimental results according to the representative eigenstate

$|\varphi_4\rangle$ and superposed state $|\omega_2\rangle$ with the definition

$$|\omega_n\rangle = N^{-1/2}\sum_{d=1}^{N}\exp\left[-\frac{2\pi i(d-1)n}{N}\right]|\varphi_d\rangle. \quad (4)$$

The expectation values of projective measurements for two such states are displayed in Figs. 4(a) and 4(b), where the filled and empty bars indicate experimental recorded coincidence counts in 60 s and theoretical calculated references, respectively. The implementation accuracy is evaluated by statistical fidelities, which are defined as $F_s(p_{\rm exp},p)=\sum\sqrt{p_{\rm exp}p}$ [38], between the theoretical and experimental probability distributions corresponding to the histograms in Figs. 4(a) and 4(b). The fidelities of these two data sets are found to be 0.98 and 0.96. The density operators reconstructed from the randomly chosen SIC POVMs are plotted in Figs. 4(c) and 4(d). The theoretical density matrices are displayed as empty bars in Figs. 4(c) and 4(d). The fidelity of the density matrix is evaluated with the formula [39]

$$F(\rho_{\rm exp},\rho)=\left|{\rm Tr}\sqrt{\sqrt{\rho}\rho_{\rm exp}\sqrt{\rho}}\right|^2, \quad (5)$$

where $\rho_{\rm exp}$ and ρ are reconstructed and reference density matrices, respectively. The fidelities are 0.853 and 0.815 for the eigenstate $|\varphi_4\rangle$ and the superposition state $|\omega_2\rangle$, respectively. It is convenient to implement complex operators in our scheme, allowing the reconstruction of a complicated density matrix with 225 nonzero complex elements. In addition to the experiment that gives the results shown in Fig. 4, three similar experiments are performed. The averaged fidelity is found to be 0.97 ± 0.02 among a total of 500 experimentally generated 15-dimensional projective operators randomly chosen from SIC POVMs. These projective operators in Eq. (3) exhibit various amplitude and phase distributions. These results suggest that our method is valid for arbitrary linear quantum operations up to 15 dimensions, and this is the first implementation of SIC POVMs on 15-dimensional photonic qudits [35].

The required number of projective measurements can be greatly reduced by use of a compressed-sensing technique. However, the reconstruction uncertainties would increase by a factor that has a negative correlation with the sampling ratio [37]. Figure 5 illustrates the measured fidelity and trace distance of the reconstructed density matrices versus the sampling ratio. Statistical results for five experimental data sets are plotted. The trace distance is calculated as $T(\rho_{\rm exp},\rho)={\rm Tr}\left[\sqrt{(\rho_{\rm exp}-\rho)^\dagger(\rho_{\rm exp}-\rho)}\right]/2$. As the generated states under test are nearly pure, the trace distance is close to the upper bound of $\sqrt{1-F(\rho_{\rm exp},\rho)^2}$.

Next, 15×15 QFT is performed, which is an important unitary quantum operation in quantum-information

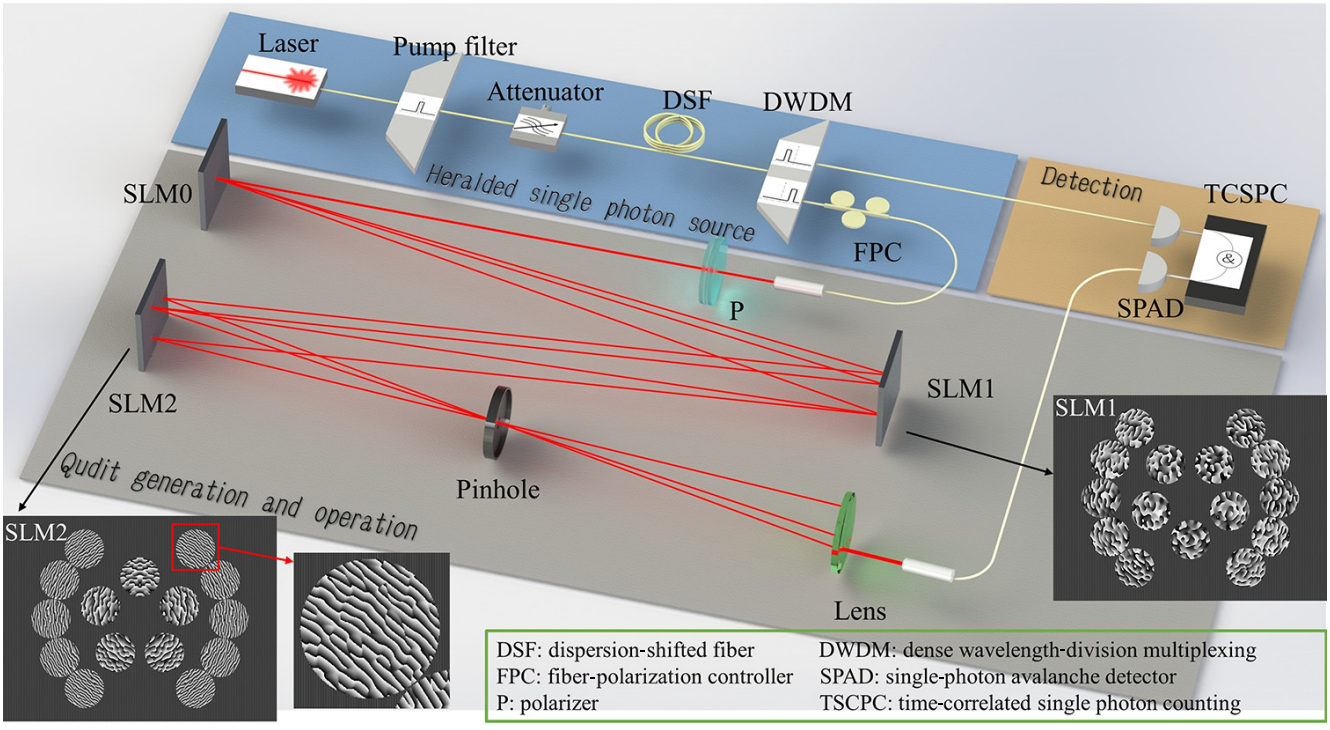

FIG. 3. Experimental setup. The insets show modulation functions on SLM1 and SLM2, together with an enlarged image of a typical phase grating.

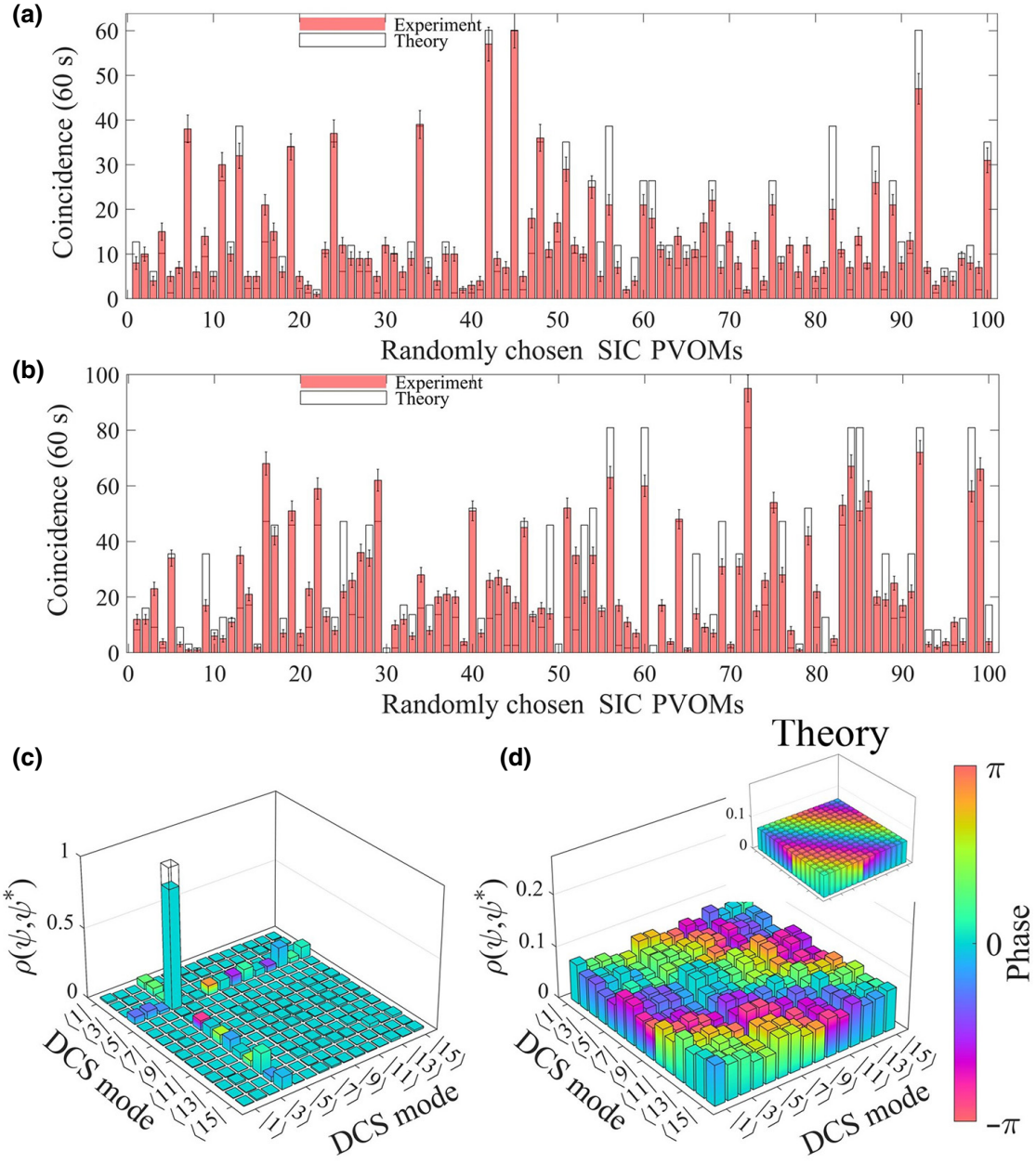

FIG. 4. Quantum-state tomography via the compressed-sensing method. (a),(b) Projective measurements. (c),(d) Reconstructed density matrices.

processing such as Shor's factorization algorithm [40]. The phase components in the experimental QFT matrix F_{exp} (with the target QFT matrix labeled F) cannot be measured directly in the computational basis $|\varphi\rangle\langle\varphi|$, and thus the fidelity of QFT is evaluated in the conjugate Fourier basis $|\omega\rangle\langle\omega|$ as defined in Eq. (4).

If the initial state $|\omega_n\rangle$ is prepared precisely, then $F|\omega_n\rangle = |\varphi_n\rangle$. Because of the orthogonal nature of the conjunctive Fourier basis, $|\langle\omega_i|\omega_j\rangle|^2 = \delta_{ij}$, the fidelity between the experimental and theoretical QFT matrices can be expressed as $F(F_{\text{exp}}, F) = F(F_{\text{exp}}\Omega, F\Omega)$, where Ω is a matrix whose nth column is $|\omega_n\rangle$. In theory, $F\Omega$ is the identity matrix acting in the computational basis $|\varphi\rangle\langle\varphi|$, and so $F_{\text{exp}}\Omega$ should approximate the identity if F_{exp} is sufficiently close to F. The experimental results for $F_{\text{exp}}\Omega$ are displayed in Fig. 6(a), which consists of coincidence counts in 120 s. The error bars are one standard deviation estimated from Poissonian counting statistics. The fidelity is calculated as 0.85 ± 0.02. The deviation from unit fidelity is caused mainly by dark-count rates of the single-photon avalanche detectors and the calibration error of the experimental setup (see the error

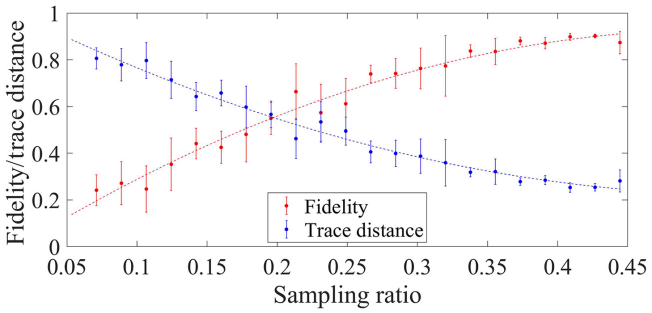

FIG. 5. Fidelity and trace distance for our reconstructed density matrix versus sampling ratio.

analysis in Appendix B). After meticulous phase calibration (explained in Appendix A 2), the fidelity could reach 0.99 with stability for 7 days for a coherent-light source; the corresponding experimental data are provided in Appendix C.

IV. EXTENSION TO PHOTON PAIRS

In this work we concentrate on single-photon operations, with each photon generated by heralding from a spontaneous parametric process. It should be possible to extend our method to manipulate both photons in an entangled pair generated from this source and so to realize high-dimensional Bell states and order-finding routines as indicated in Figs. 6(b) and 6(c). Our investigations suggest that it should be possible to generate and manipulate such states with a large Schmidt number K of approximately 40 [16]. The spatial entangled state $\sum |x\rangle|x\rangle$ is one of the high-dimensional generalized Bell states. By acting on this with a high-dimensional $\hat{X}$ gate on one photon and a corresponding $\hat{Z}$ gate on its partner, the Bell state can be switched to any another state for applications such as quantum teleportation of qudits [41]. The two-photon gates used in linear optical quantum-information processing are nondeterministic in nature [11]. For this reason we propose an alternative procedure for the order-finding routine in Shor's factorization algorithm. This scheme, which avoids two-photon operations, is depicted in Fig. 6(c). High-dimensional QFT and a compiled modular exponential function (MEF) [42] are applied on twin beams resulting from SPDC, respectively. The optical nonlinear process could provide a large-enough state space for further demonstration [25]. Furthermore, our scheme is also suitable for indistinguishable multiphoton manipulation, including boson sampling [18].

We begin our discussion with an analysis of the extent to which the distinct paths in our scheme are distinguishable. The optical path differences induced during propagation from SLM1 to SLM2 are compensated in Eq. (A6). The phase compensation is valid when the coherence length of photons is greater than the optical path differences. In this demonstration, the distance between SLM1 and SLM2 is 0.8 m, while the maximum and average distances between DCS modes in the transverse plane are approximately 5 mm and approximately 1 mm, respectively. This leads to a maximum optical path difference of approximately 20 times the optical wavelength, which is 30 μm and the corresponding time delay is 0.1 ps. The average optical path difference is about one wavelength. The influences of optical path differences will be sufficiently small when the linewidths of the pump filter and signal (idler) filter are much narrower than 10 THz (0.1 ps^{-1}). Thus, our scheme is suitable for indistinguishable multiphoton manipulation, including boson sampling [18].

When the transverse coordinates of the spatial-encoding basis are considered as distributed on a single circle, the two-photon spatial-mode-entangled state generated via frequency-degenerate type-I SPDC can be expressed as $\sum_{x=0}^{N-1} |x\rangle|x\rangle$. This is a consequence of transverse momentum conservation or phase matching in the source crystal, and N should not exceed the Schmidt number K of the transverse momentum entanglement. According to Ref. [16], the closed form of the Schmidt number is

$$K = \frac{1}{4}\left(b\sigma + \frac{1}{b\sigma}\right)^2, \tag{6}$$

where σ and b^{-1} are the widths of Gaussians. For the biphoton amplitude distribution of the type-I SPDC cone shown in Fig. 6, the amplitudes of b^{-1} and σ are proportional to the radius and thickness of the SPDC cone, respectively. With this estimation, the Schmidt number K for our SPDC source is approximately 40, and this sets a limit on the dimensionality achievable in future experiments. We present two experimental proposals for our linear operation scheme and entangled-photon source.

A. Compiled demonstration of Shor's factorization algorithm

The difficulty in factoring a composite number $M = pq$ is believed to be equivalent to that of finding the period r of the MEF $f(x) = a^x \pmod M$, where a can be chosen to be any integer. Shor's algorithm provides an efficient routine [38–40,42,43] to find the period r, where "quantum parallelism" can be achieved by coherent manipulation and detection of the highly entangled state:

$$\frac{1}{\sqrt{N}} \sum_{x=0}^{N-1} |x\rangle|\mathrm{mod}(a^x, M)\rangle. \tag{7}$$

The value of N denotes the size of each quantum-register set. We proceed by applying QFT of dimensionality N to the first register, which produces quantum interference from which information about period r of $f(x)$ can be

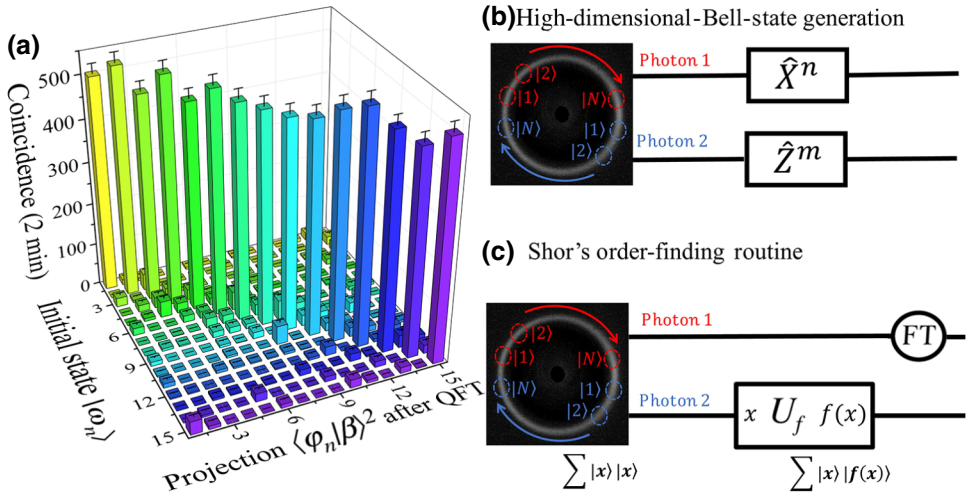

FIG. 6. QFT with dimensionality of 15×15 tested with the conjugate Fourier basis. (b) Illustration for generation of high-dimensional Bell states and (c) equivalent order-finding routine with high-dimensional entangled photons, where $f(x) = 2^x \pmod N$ denotes a modular exponential function. A type-I SPDC cone photographed by a near-infrared CMOS camera is shown.

deduced [42]:

$$\frac{1}{N}\sum_{y=0}^{N-1}\sum_{x=0}^{N-1} e^{2\pi ixy/N}|y\rangle|\mathrm{mod}(a^x, M)\rangle. \tag{8}$$

Thus, the preparation of the state in Eq. (8) is an essential element for demonstrating Shor's algorithm.

The initial states of two quantum registers are separable ground states in the original order-finding routine [40]. The state in Eq. (7) may be realized by multiphoton execution that entangles N input values of x in the first register with the corresponding value $f(x)$ in the second register. However, with initial entangled state $\sum_{x=0}^{N-1}|x\rangle|x\rangle$ in our proposal, there is no need to generate entanglement with multiphoton-controlled gates, which would lead to low probability of success with postselection [11]. Instead, we proceed by acting with the QFT on the first quantum register to produce the state

$$\frac{1}{N}\sum_{y=0}^{N-1}\sum_{x=0}^{N-1} e^{2\pi ixy/N}|y\rangle|x\rangle. \tag{9}$$

We recognize this transformation as one of our linear operators applied to the first photon. Next, the MEF is applied on the second quantum register. Thus, the state in Eq. (8) is prepared and quantum parallelism can be exhibited by simultaneous readout of the two registers. Although the MEF is a nonlinear operation and cannot be implemented directly with any linear operation scheme, a proof-of-principle experiment of Shor's algorithm would be feasible since the pre-compiled MEF [42] could be performed by linear transformation with linear optical elements. As a concrete example, with $N = 16$ for the number of samplings on the SPDC cone and the dimensionality of the QFT, a factorization of $15 = 3 \times 5$ can be demonstrated. Additionally, such an implementation would not be limited to the "easy" case [42,44] of $a = 11$ that was previously reported with a photonic platform.

It is significant that a high-dimensional entangled state is used as the initial state, and thus multiphoton-controlled gates are avoided. Because of the high-dimensional encoding, only one photon is needed for each quantum register, and thus the coherent manipulation and detection can be further simplified.

B. Generation of complete high-dimensional Bell basis

The complete high-dimensional Bell basis can be generated with our technique. The N-dimensional Bell basis can be written as [41,45]

$$|\psi\rangle_{mn} = \frac{1}{\sqrt{N}}\sum_{x=0}^{N-1} e^{2\pi ixn/N}|x\rangle|\mathrm{mod}(x+m, N)\rangle. \tag{10}$$

We begin with the initial state sampled from the SPDC cone. We have one of the N-dimensional Bell states:

$$|\psi\rangle_{00} = \frac{1}{\sqrt{N}}\sum_{x=0}^{N-1}|x\rangle|x\rangle. \tag{11}$$

With N-dimensional shift matrices and clock matrices applied to the second photon, the Bell state $|\psi\rangle_{00}$ can be transformed into $|\psi\rangle_{m0}$ and $|\psi\rangle_{0n}$, respectively. Here the shift matrices and clock matrices have the forms

$$T_{\mathrm{shift},m} = \frac{1}{\sqrt{N}}\sum_{x=0}^{N-1}|\mathrm{mod}(x+m, N)\rangle\langle x|, \tag{12}$$

$$T_{\mathrm{clock},n} = \frac{1}{\sqrt{N}}\sum_{x=0}^{N-1} e^{2\pi ixn/N}|x\rangle\langle x|. \tag{13}$$

The state $|\psi\rangle_{00}$ can then be transformed into any target Bell state $|\psi\rangle_{mn}$ by applying a product of $T_{\mathrm{shift},m}$ and $T_{\mathrm{clock},n}$ to

the second photon. Thus, the complete N-dimensional Bell basis can be generated by type-I SPDC combined with our linear operation scheme. Furthermore, unit success probability can be achieved, at least in principle, when shift matrices and clock matrices are used, as well as any of their products. As a concrete example, a 15-dimensional complete Bell basis can be generated with our proposed 15×15 arbitrary matrix transformations. As maximally entangled two-particle quantum states, the complete Bell basis could be used for high-dimensional quantum protocols such as teleportation, dense coding, and entanglement swapping.

V. DISCUSSION AND CONCLUSIONS

Our results can be compared with recent developments achieved with multiplane light conversion [26,46]. Using our method, we are able to work with a significantly higher dimension of state space. Moreover, we avoid a cascaded structure and, with it, the requirement for an increase in the number of elements as the dimensionality increases, albeit with a penalty in efficiency.

Before summarizing, we provide some details on the efficiency, reliability, and dimensionality of our scheme. An efficiency factor of $1/N$ is incurred in the spatial filtering by the pinhole in the worst case of an $N \times N$ demonstration as previously discussed [29]. The intrinsic loss is determined by the average number of nonzero elements in each row of the target matrix. Our scheme would be lossless for $\hat{X}$ gates and $\hat{Z}$ gates that could be used to construct any unitary transformations [6]. In the 15×15 QFT demonstration, the total insertion loss is measured to be 21.2 dB. This arises from the theoretical loss of approximately 13.7 dB, estimated by the factor $1/N$, the imperfect phase-grating efficiency shown in Fig. 2(b), and an additional loss of 7.5 dB due to the modulation efficiency and reflection rate of two SLMs.

The intrinsic loss of $1 - 1/N$ is the inevitable penalty paid to avoid a cascaded structure. Against this, for our simple noncascading structure, the attenuation induced by the optical elements should be largely independent of the dimensionality of the linear operator realized. Moreover, our scheme exhibits robustness with regard to phase-modulation errors compared with a cascaded design [29].

The quantum operators realized here are demonstrated with a dimensionality of 15, but an extension of the 24-dimensional arbitrary linear transformation was demonstrated previously [29]. In principle, the achievable dimensionality is limited only by the achievable spatial resolution of phase modulation. Our method is not limited to SLMs. Any passive holographic elements able to perform the phase modulation would be possible, including specially engineered metasurfaces [47]. Thus, it should be possible to realize an on-chip high-dimensional quantum operator with our scheme.

In summary, we proposed and demonstrate a simple and flexible scheme to perform arbitrary linear quantum operations with high fidelity and high dimensionality. SIC POVMs and QFT are performed with a dimensionality of 15×15. Since DCS modes are used, we believe that our work will have potential to fully explore SPDC in high-dimensional quantum applications, including switching of Bell states, and is also compatible with operating path-encoded qudits.

ACKNOWLEDGMENTS

This work was supported by the National Key Research and Development Program of China (Grants No. 2017YFA0303700 and No. 2018YFB2200402), the National Natural Science Foundation of China (Grants No. 61875101 and No. 61621064), the Beijing Innovation Center for Future Chips, and the Beijing Academy of Quantum Information Science. S.L. thanks Peng Zhao, Xin Yao, and Rong Xue for valuable discussions and helpful comments. S.M.B. thanks the Royal Society for support through Grants No. RP/150122 and No. RP/EA/180010.

APPENDIX A: ENCODING METHOD USING SPATIAL LIGHT MODULATORS

The spatial resolution of the SLM used (Holoeye Pluto series) is 1920×1080, while the size of each single pixel is about 8×8 μm^2. Firstly, we introduce some ancillary phase-modulation patterns to simplify the following explanation.

1. Phase-modulation functions

As mentioned in the main text, the modulation efficiency of SLMs is less than unity. To separate effectively the components directly reflected without modulation, first-order diffraction is used, and the phase-modulation function is

$$F_{\text{grating}}(\mathbf{r}) = \exp(i\mathbf{k}_{\text{grating}} \cdot \mathbf{r}). \tag{A1}$$

With the help of such blazed gratings, the directly reflected components can be spatially filtered out. In this work, the transverse wave vector $\mathbf{k}_{\text{grating}}$ is selected to obtain a blazed grating with a spatial period of four pixels.

To maintain the transverse size of Gaussian spots against natural divergence during propagation, a symmetric confocal cavity is implemented between SLM1 and SLM2 by a Fresnel lens programmed on the SLMs. Under the paraxial approximation, the transmission function of a lens with focal length f is

$$F_{\text{lens}}(\mathbf{r}) = \exp\left(\frac{ik|\mathbf{r}|^2}{2f}\right). \tag{A2}$$

Additionally, a binary function is used to avoid spatial coincidences of phase gratings acting on different Gaussian

spots $|\varphi_n\rangle$. The expression is

$$\chi(\mathbf{r}) = \begin{cases} 1, & |\mathbf{r}| < R_{\text{threshold}}, \\ 0, & \text{otherwise.} \end{cases} \tag{A3}$$

The value of $R_{\text{threshold}}$ is determined according to the beam waist of a single Gaussian spot. The amplitude modulation is implemented by a checkerboard method. The phase modulation on SLM0 is settled as

$$F_{\text{diff0}}(\mathbf{r}) = \exp\left\{ i \arg\left[\sum_{n=1}^{N} \xi_n a_n \exp(i\mathbf{k_n} \cdot \mathbf{r}) \right] \right\} \times F_{\text{lens}}(\mathbf{r}) \chi(\mathbf{r}) F_{\text{grating}}(\mathbf{r}), \tag{A4}$$

where $\{a_n\}$ is the state vector of the initial state and $\{\xi_n\}$ are optimization parameters to ensure the desired beam splitting. The transverse wave vectors $\{\mathbf{k}_n\}$ determine the propagation directions of the initial Gaussian spots and they are used to mimic the SPDC cones produced in a nonlinear crystal. Under the paraxial approximation, the definition of $\{\mathbf{k}_n\}$ is

$$\mathbf{k}_n = \frac{k\mathbf{R}_n}{2f} \quad \text{for all } n = 1, \ldots, N. \tag{A5}$$

The transverse coordinate of the nth Gaussian spot is $\mathbf{R}_n$ as mentioned in the main text. The phase modulation on SLM1 is chosen to be

$$F_{\text{diff1}}(\mathbf{r}) = \sum_{m=1}^{N} \exp\left(i \arg\left\{ \sum_{n=1}^{N} \mu_{mn} A_{mn} \times \exp[i(\mathbf{k}_{mn} - \mathbf{k}_m) \cdot (\mathbf{r} - \mathbf{R}_m) - i\theta_{mn}] \right\} - i\delta_m \right) \times F_{\text{lens}}(\mathbf{r} - \mathbf{R}_m) \chi(\mathbf{r} - \mathbf{R}_m) \times F_{\text{grating}}(\mathbf{r}). \tag{A6}$$

The parameters μ_{mn}, A_{mn}, and $\mathbf{k}_{mn}$ in Eq. (A6) have the same definitions as those in the main text. As the optical path of each spot is different during propagation from SLM1 to SLM2, the phase compensation θ_{mn} should also be different for each splitting direction and can be expressed as

$$\theta_{mn} = \frac{k|\mathbf{R}_n - \mathbf{R}_m|^2}{4f}. \tag{A7}$$

Similarly, a different phase compensation δ_m is used for each initial Gaussian spot to compensate for the path difference during propagation from SLM0 to SLM1. The value of δ_m is selected to be

$$\delta_m = \frac{k|\mathbf{R}_m|^2}{4f}. \tag{A8}$$

In addition to beam splitting and the focusing lens, extra beam-refraction functions are also used in Eq. (A6) to compensate for the initial transverse wave vectors $\{\mathbf{k}_n\}$ associated with each individual Gaussian spot generated by SLM0.

The function of SLM2 is beam recombination. This is the reverse procedure of beam splitting, and so the phase-modulation functions are similar to those on SLM1. The phase modulation required on SLM2 is

$$F_{\text{diff2}}(\mathbf{r}) = \sum_{m=1}^{N} \exp\left(i \arg\left\{ \sum_{n=1}^{N} \nu_{mn} B_{mn} \times \exp[-i\mathbf{k}_{mn} \cdot (\mathbf{r} - \mathbf{R}_m)] \right\} \right) \times F_{\text{lens}}(\mathbf{r} - \mathbf{R}_m) \chi(\mathbf{r} - \mathbf{R}_m) \times F_{\text{lens}}(\mathbf{r}) F_{\text{grating}}(\mathbf{r}). \tag{A9}$$

The parameters ν_{mn}, B_{mn}, and $\mathbf{k}_{mn}$ in Eq. (A9) have the same definition as those in the main text. In contrast with the phase modulation on SLM1, there is no need for extra additional refraction and phase compensation on SLM2, but an extra lens is required for the last step, which is beam filtering with a pinhole. A pinhole with a transmission function described by $\chi(\mathbf{r})$ is positioned one focal length f after SLM2. To accomplish beam filtering, a lens with focal length f is placed one focal length away from the pinhole, as presented in the experimental setup in the main text.

2. Phase-calibration method

In the laboratory implementation, phase errors arise from the misalignment of optical elements. In addition, there will be extra phase errors if the phase-compensation terms in Eq. (A6) are not estimated precisely. Fortunately, these phase errors are constant and independent of the target matrices. Thus, the phase errors can be corrected before the experiments are performed. The amplitudes of the matrix elements are robust with regard to misalignment and there is no need for amplitude calibration in most situations.

The phase calibration is performed with a laser source (RIO ORION) centered at 1550 nm in place of the heralded single-photon source in the experimental setup. The final state after linear operation is measured by a CCD camera. Generally, the influence of constant phase error ϵ on the

implemented matrix transformation T^{real} is given by

$$T^{\text{real}}_{mn} = T_{mn}\exp(i\epsilon_{mn}). \tag{A10}$$

The error matrix $\exp(i\epsilon_{mn})$ is measured so that the phase errors can be compensated by implementation of $T_{mn}\exp(-i\epsilon_{mn})$ rather than T_{mn}. Any matrix with no zero elements could be used for phase calibration. In our experiments, discrete Fourier transformation (DFT) is performed without phase calibration first. Then, the phase terms of all elements in the realized DFT are measured. Finally, the error matrix $\exp(i\epsilon_{mn})$ is deduced by our comparing the achieved DFT and the standard DFT. A tomographic method is used to measure the phase terms. By measuring the amplitudes of the output vectors corresponding to meticulously designed input vectors, we can deduce the phase terms of the transformation matrix. Here the calibration principle is shown with the example of a 3×3 matrix:

$$\begin{pmatrix} O_{11} & O_{12} & O_{13} & O_{14} \\ O_{21} & O_{22} & O_{23} & O_{24} \\ O_{31} & O_{32} & O_{33} & O_{34} \\ O_{41} & O_{42} & O_{43} & O_{44} \end{pmatrix} = T^{\text{real}}_{3\times 3} \times \begin{pmatrix} 1 & 1 & i & i \\ 1 & 0 & 1 & 0 \\ 0 & 1 & 0 & 1 \end{pmatrix}. \tag{A11}$$

The results for interference of matrix elements in the first column with elements in the other columns are available as the intensities in the output vectors. To calculate the relative phase with respect to elements in the first column precisely, the inner product is obtained twice. For example, the phase of T^{real}_{12} can be found from

$$\begin{aligned} I^{\cos}_{12} &= |O_{11}|^2 = |T^{\text{real}}_{11} + T^{\text{real}}_{12}|^2, \\ I^{\sin}_{12} &= |O_{13}|^2 = |iT^{\text{real}}_{11} + T^{\text{real}}_{12}|^2. \end{aligned} \tag{A12}$$

As the amplitudes of elements in T^{real} are known, the relative phases can be deduced from Eq. (A12) without any ambiguity. Generally, $2(N-1)$ tests with different input vectors are required to measure all the relative phase terms of the $N \times N$ matrix.

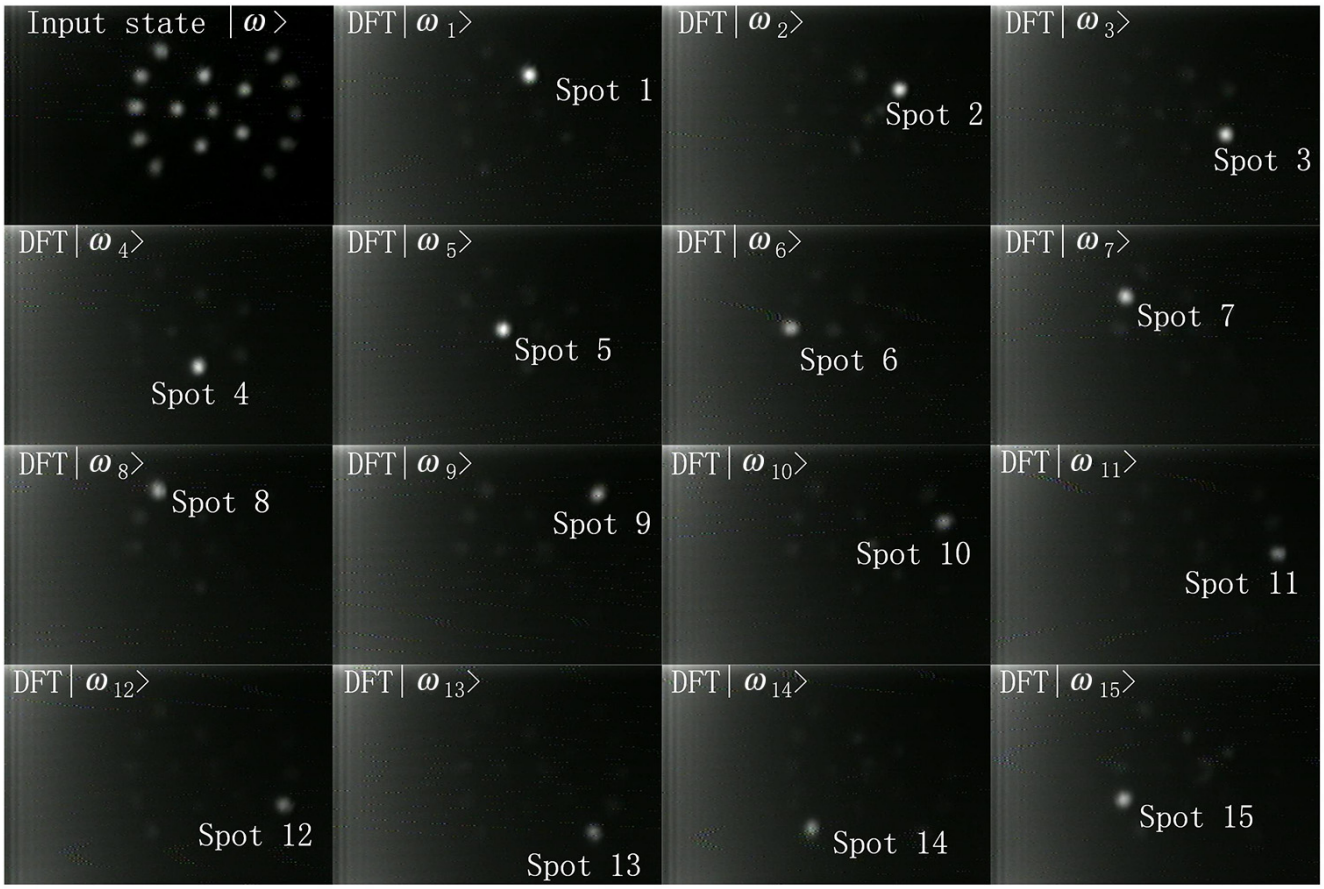

FIG. 7. The results for the calibrated DFT matrix under a Fourier basis. For different input Fourier states, the output of the DFT matrix will be single Gaussian spots in different positions.

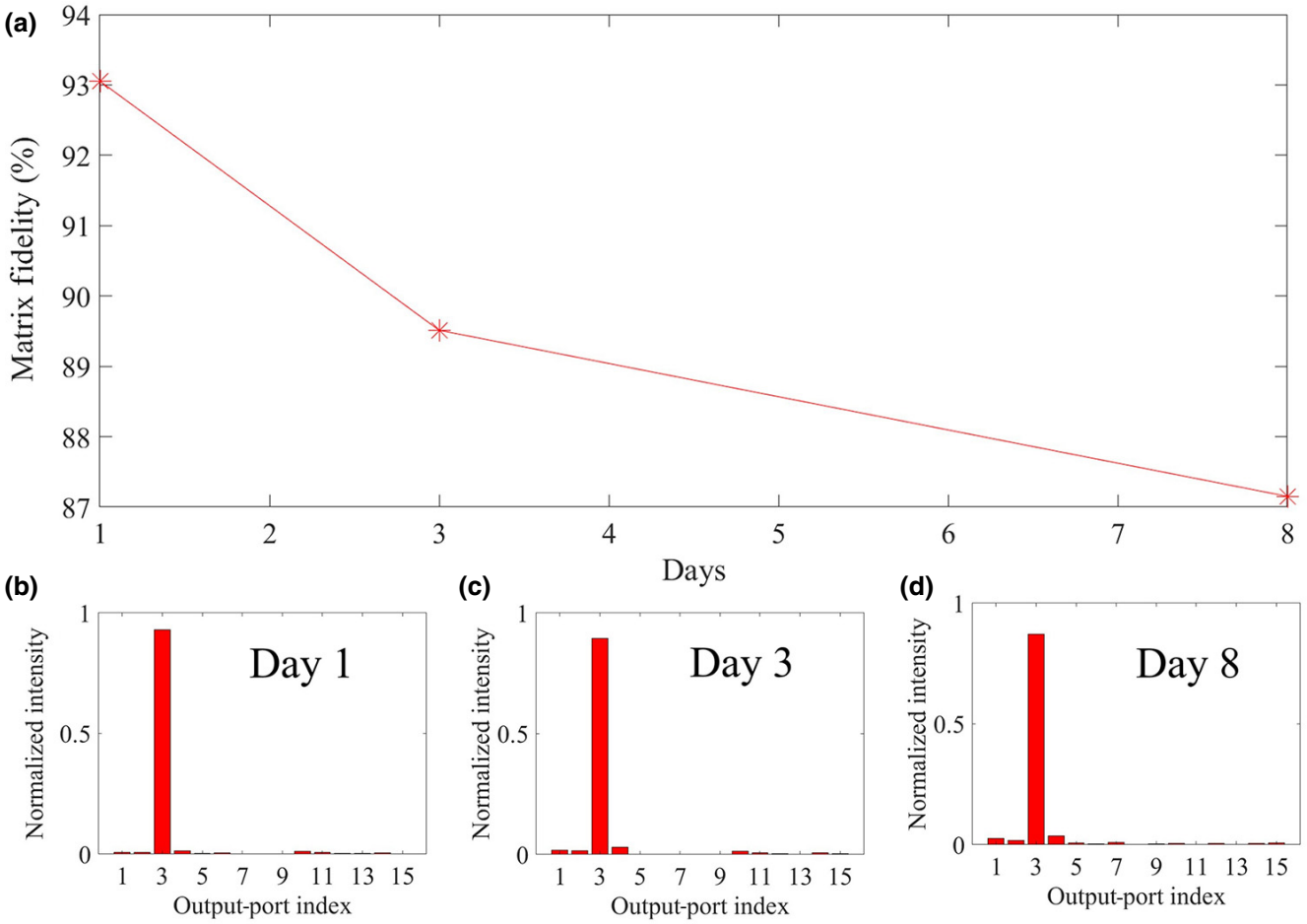

FIG. 8. (a) Matrix-fidelity variation of the calibrated 15 × 15 DFT demonstration over 1 week. (b)–(d) Output vector of DFT with the input Fourier basis state $|\omega_3\rangle$.

There would be, however, a constant relative phase between different rows of the matrix that is not calibrated. These relative phase terms can be considered as path differences from each output port of the transformation to its corresponding detector. Thus, these phase terms have no influence in quantum computational tasks, including multiphoton interference such as boson sampling.

It is possible to handle these phase differences among the matrix rows via a different method for phase measurement as introduced in our previous work [29], where a reference field is required. However, the tomographic method used in this work is simpler and more accurate. The test results for the calibrated DFT matrix acting on the Fourier basis are shown in Fig. 7. The input and output state vectors are captured by the CCD camera. All the input Fourier bases $|\omega_n\rangle$ have uniform amplitude but different phase distributions. For different input Fourier basis states, the output of the DFT matrix would be single Gaussian spots in different positions. Each time only one output port is bright, while other output ports vanish due to multiport interference, as they should. The stability of our calibration method is tested over a period of 1 week. The fidelity of the 15 × 15 DFT demonstration is selected as an example. As shown in Fig. 8, the fidelity drops from approximately 93% to approximately 87% after 7 days with no further calibration. Once the calibration is performed, because the constant phase error is independent of the transformation matrices, any target matrices can be readily implemented with high fidelity.

APPENDIX B: ERROR ANALYSIS

The errors can be categorized as follows: (i) errors introduced by the TCSPC, (ii) errors in the design and implementation of the modulation functions on the SLMs, and (iii) imperfections in matrix calibration. Among these, the dominant one is introduced by TCSPC due to the Poissonian counting statistics and dark counts in the detector. The errors of the parameters in thew SLM modulation functions as well as imperfections in matrix calibration

lead to only a small loss of fidelity for the implemented linear operators and projectors.

1. Errors induced by TCSPC

The raw photon-counting rate of the heralded single-photon source is about 270 Hz with IDQ220 detectors. However, the total insertion loss of the experimental setup is approximately 32 dB, including polarization control, high-dimensional state generation, linear operation, and free-space-to-fiber coupling. In addition to the intrinsic loss of 13.76 dB to implement a 15×15 matrix, there is an extra loss of 7.52 dB caused by the nonunit modulation efficiency of SLM1 and SLM2. Furthermore, additional losses of 3.01, 4.46, and 4.15 dB are induced by polarization control as well as fiber-to-free-space collimation, state generation with SLM0, and free-space-to-fiber collection, respectively. As shown in the main text, the data-accumulation time for each measurement is 1 min, and hence only tens of coincidence events can be recorded. As the single-photon events follow the Poisson distribution, the uncertainty is approximately $\sqrt{N_{\text{count}}}$ for data series. When N_{count} is low, the relative uncertainty of coincidence counting increases and is the main reason for fidelity deterioration in our quantum projective measurements. To further confirm this, we perform high-dimensional state tomography with the same projective method but with a classical coherent-light source in place of our SPDC source. The results for SIC POVMs as well as reconstruction of density matrices are presented in Fig. 10 in Appendix C. For four groups of experiments, the statistical fidelities of the SIC POVMs are 0.979–0.996, while the fidelities of the density matrices are 0.930–0.994. With an intense light source, the decrease in the errors is clear. This supports our conclusion that the uncertainty of coincidence counting is the critical error in this demonstration.

The compressed-sensing technique will further amplify the uncertainties. According to compressed-sensing theory [37], the error ε_{DM} of the reconstructed density matrix follows

$$\varepsilon_{\text{DM}} \geq \left(\sqrt{N^2/m}\right)\varepsilon_p, \tag{B1}$$

where N is the dimensionality of the density matrix, m is the number of projective measurements, and ε_p is error of projection values. As the sampling ratio is about 0.35 in this work, the errors of the density matrices will be at least approximately 1.7 times the errors of the raw projection data, which could explain the fidelity deterioration from quantum projection values to density matrices.

The accidental coincidence rate caused by dark counts in the single-photon detectors is measured to be approximately 2 min^{-1}. The fidelity deterioration of the DFT results in the main text is caused mainly by dark counts occurring in those output ports that should be quenched due to destructive interference of a single photon.

2. Errors induced by modulation functions on SLMs

In principle, the phase-only modulation functions should be modified by optimization parameters μ_{mn} and ν_{mn} in Eqs. (A6) and (A9) to achieve unit fidelity. However, it is highly time-consuming to optimize the phase gratings every time for different tasks and after phase calibration. Moreover, as mentioned in the main text, near-unit fidelity can be achieved even by directly setting $\{\mu_{mn}\}$ and $\{\nu_{mn}\}$ to 1. This allows fast design of phase-modulation functions to realize a general target matrix if the fidelity deterioration induced can be ignored.

To quantify the influence of the optimization parameters, we mathematically model our experimental setup so that it can be simulated according to the Huygens-Fresnel theorem within the paraxial approximation. In this way, we can characterize the theoretical fidelity of matrix transformations under all the experimental conditions, including beam splitting, beam recombining, free-space propagation, and spatial filtering. One thousand unitary matrices are randomly generated with a dimensionality of 15×15. The phase-modulation functions for these matrices are designed according to Eqs. (A6) and (A9) with all the optimization parameters equal to 1. Figure 9 presents the fidelity histogram of 1000 numerical simulation trials. The standard derivation of the fidelity is calculated as $\delta F < 1.5 \times 10^{-4}$. The high fidelities and the small fidelity derivation suggest that the fidelity deterioration without optimization is negligible.

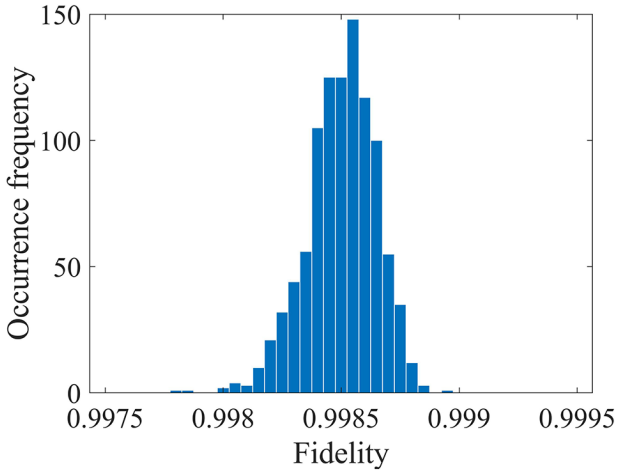

FIG. 9. Histogram for normalized fidelity of different unitary matrices with dimensionality of 15×15. The phase gratings are not optimized in these designs. The histogram is obtained through Monte Carlo simulation with 1000 trials.

3. Errors induced by matrix calibration

Matrix calibration is performed with a laser source centered at 1550 nm, which is close to the central wavelength of the signal filter for single photons, which is 1549.3 nm. As SLMs are not narrowband devices, these two wavelengths can be considered as the same for the purposes of phase calibration.

During phase calibration, the amplitudes of the matrix elements are supposed to be accurate. The simulated results shown in Fig. 9 support this assumption. The intensities of the output states are measured by an (In,Ga)As CCD camera. The nonlinear effects as well as the background noise of the CCD camera will also induce some errors, which are mostly responsible for the fidelity difference of the experimental results with intense light presented in Fig. 10.

APPENDIX C: ADDITIONAL TOMOGRAPHY RESULTS

The experimental results for state tomography with a classical laser source are presented in Fig. 10. Compressed-sensing quantum-state tomography results with a different sampling ratio are displayed in Fig. 11. Figure 10 presents four groups of experimental results. The three columns in Fig. 10 indicate results for SIC POVMs, experimental density matrices, and theoretical density matrices, respectively. Figure 10(a) presents the characterization for the single-mode eigenstate, while Figs. 10(b)–10(d) present the characterization for the superposed states. For Figs. 10(a)–10(d), the statistical fidelities of the SIC POVMs are 0.996, 0.985, 0.979, and 0.981, while the fidelities for state tomography are 0.994, 0.946, 0.930, and 0.940.

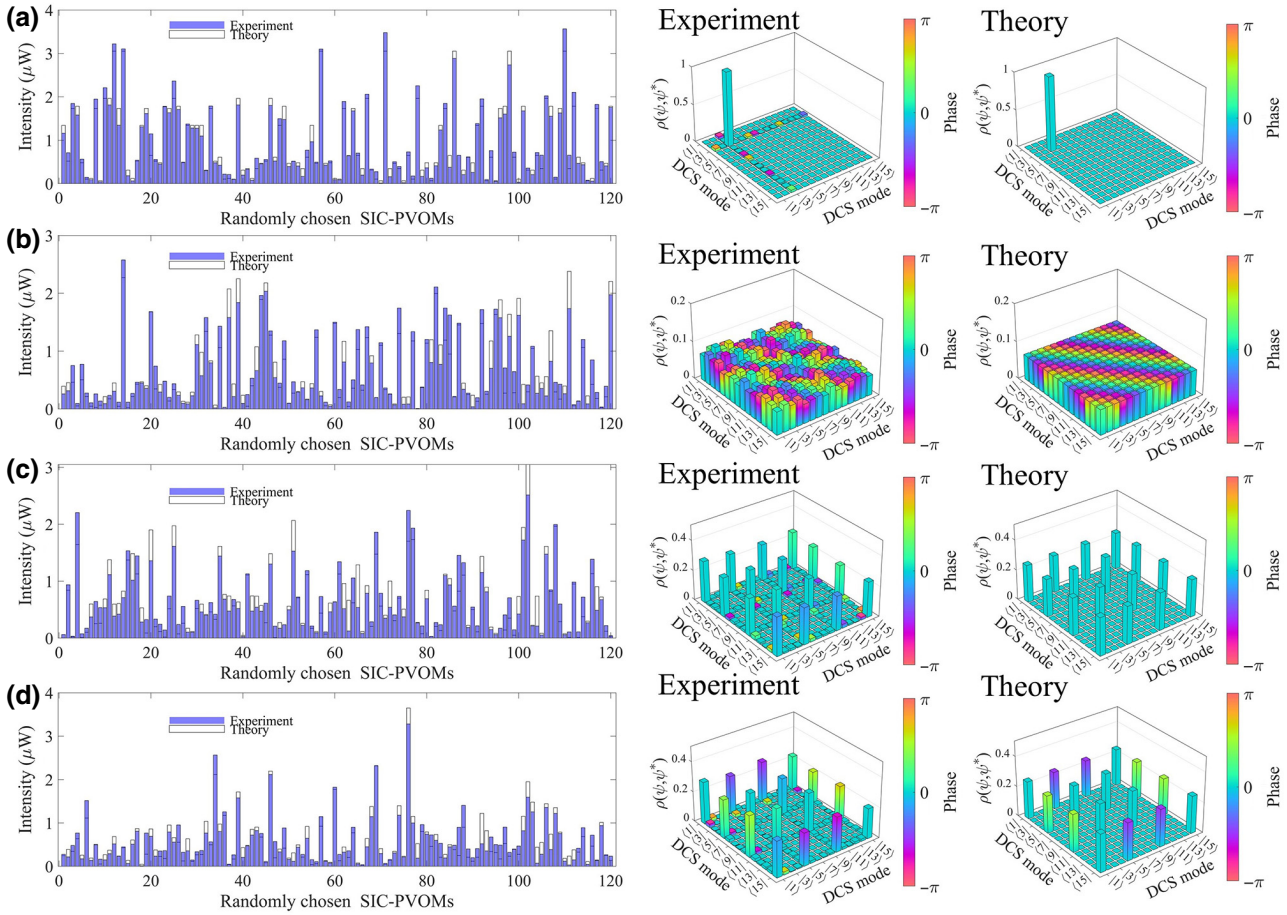

FIG. 10. Four groups of state tomography with a classical coherent-light source. The three columns correspond to the results for SIC POVMs, experimental density matrices, and theoretical density matrices, respectively. (a) Results for a single-mode eigenstate. (b)–(d) Results for superposed states. The phase information for matrix elements with modulus $|\rho_{ij}| < 0.02$ is approximately randomly distributed and not displayed to aid clarity.

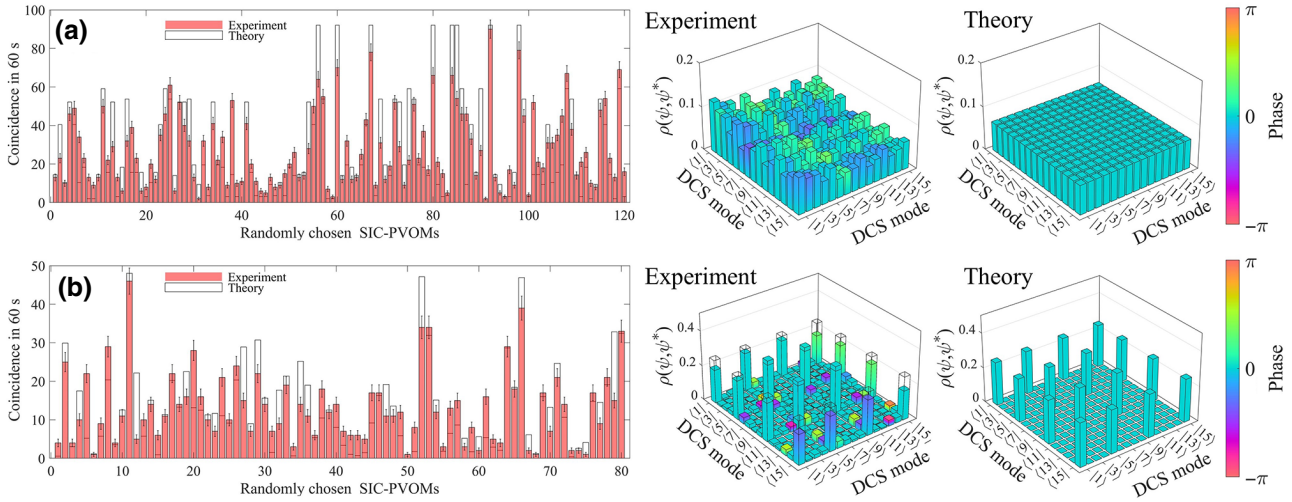

FIG. 11. Two groups of quantum projective measurements and quantum-state tomography. The three columns correspond to the results for SIC POVMs, experimental density matrices, and theoretical density matrices, respectively. The statistical fidelities of SIC POVMs are 0.934 (a) and 0.936 (b). The fidelities of quantum-state tomography are 0.806 and 0.738.

[1] J.-W. Pan, Z.-B. Chen, C.-Y. Lu, H. Weinfurter, A. Zeilinger, and M. Żukowski, Multiphoton entanglement and interferometry, Rev. Mod. Phys. **84**, 777 (2012).

[2] P. G. Kwiat, K. Mattle, H. Weinfurter, A. Zeilinger, A. V. Sergienko, and Y. Shih, New High-Intensity Source of Polarization-Entangled Photon Pairs, Phys. Rev. Lett. **75**, 4337 (1995).

[3] A. Mair, A. Vaziri, G. Weihs, and A. Zeilinger, Entanglement of the orbital angular momentum states of photons, Nature **412**, 313 (2001).

[4] M. Kues, C. Reimer, P. Roztocki, L. R. Cortés, S. Sciara, B. Wetzel, Y. Zhang, A. Cino, S. T. Chu, B. E. Little, D. J. Moss, L. Caspani, J. Azaña, and R. Morandotti, On-chip generation of high-dimensional entangled quantum states and their coherent control, Nature **546**, 622 (2017).

[5] M. Reck, A. Zeilinger, H. J. Bernstein, and P. Bertani, Experimental Realization of any Discrete Unitary Operator, Phys. Rev. Lett. **73**, 58 (1994).

[6] A. Babazadeh, M. Erhard, F. Wang, M. Malik, R. Nouroozi, M. Krenn, and A. Zeilinger, High-Dimensional Single-Photon Quantum Gates: Concepts and Experiments, Phys. Rev. Lett. **119**, 180510 (2017).

[7] H.-H. Lu, J. M. Lukens, N. A. Peters, O. D. Odele, D. E. Leaird, A. M. Weiner, and P. Lougovski, Electro-Optic Frequency Beam Splitters and Tritters for High-Fidelity Photonic Quantum Information Processing, Phys. Rev. Lett. **120**, 030502 (2018).

[8] J. Bavaresco, N. Herrera Valencia, C. Klöckl, M. Pivoluska, P. Erker, N. Friis, M. Malik, and M. Huber, Measurements in two bases are sufficient for certifying high-dimensional entanglement, Nat. Phys. **14**, 1032 (2018).

[9] J. Wang, S. Paesani, Y. Ding, R. Santagati, P. Skrzypczyk, A. Salavrakos, J. Tura, R. Augusiak, L. Mančinska, D. Bacco, D. Bonneau, J. W. Silverstone, Q. Gong, A. Acín, K. Rottwitt, L. K. Oxenløwe, J. L. O'Brien, A. Laing, and M. G. Thompson, Multidimensional quantum entanglement with large-scale integrated optics, Science **360**, 285 (2018).

[10] T. Brougham, C. F. Wildfeuer, S. M. Barnett, and D. J. Gauthier, The information of high-dimensional time-bin encoded photons, Eur. Phys. J. D **70**, 214 (2016).

[11] E. Knill, Quantum gates using linear optics and postselection, Phys. Rev. A **66**, 052306 (2002).

[12] J. Carolan, C. Harrold, C. Sparrow, E. Martin-Lopez, N. J. Russell, J. W. Silverstone, P. J. Shadbolt, N. Matsuda, M. Oguma, M. Itoh, G. D. Marshall, M. G. Thompson, J. C. F. Matthews, T. Hashimoto, J. L. O'Brien, and A. Laing, Universal linear optics, Science **349**, 711 (2015).

[13] P. Imany, J. A. Jaramillo-Villegas, M. S. Alshaykh, J. M. Lukens, O. D. Odele, A. J. Moore, D. E. Leaird, M. Qi, and A. M. Weiner, High-dimensional optical quantum logic in large operational spaces, npj Quantum Inf. **5**, 59 (2019).

[14] A. Martin, T. Guerreiro, A. Tiranov, S. Designolle, F. Fröwis, N. Brunner, M. Huber, and N. Gisin, Quantifying Photonic High-Dimensional Entanglement, Phys. Rev. Lett. **118**, 110501 (2017).

[15] A. Rossi, G. Vallone, A. Chiuri, F. De Martini, and P. Mataloni, Multipath Entanglement of Two Photons, Phys. Rev. Lett. **102**, 153902 (2009).

[16] C. K. Law and J. H. Eberly, Analysis and Interpretation of High Transverse Entanglement in Optical Parametric Down Conversion, Phys. Rev. Lett. **92**, 127903 (2004).

[17] M. V. Fedorov, Azimuthal entanglement and multichannel Schmidt-type decomposition of noncollinear biphotons, Phys. Rev. A **93**, 033830 (2016).

[18] H. Wang, Y. He, Y.-H. Li, Z.-E. Su, B. Li, H.-L. Huang, X. Ding, M.-C. Chen, C. Liu, J. Qin, J.-P. Li, Y.-M. He, C. Schneider, M. Kamp, C.-Z. Peng, S. Höfling, C.-Y. Lu, and J.-W. Pan, High-efficiency multiphoton boson sampling, Nat. Photon **11**, 361 (2017).

[19] N. C. Harris, G. R. Steinbrecher, M. Prabhu, Y. Lahini, J. Mower, D. Bunandar, C. Chen, F. N. C. Wong, T. Baehr-Jones, M. Hochberg, S. Lloyd, and D. Englund, Quantum transport simulations in a programmable nanophotonic processor, Nat. Photon **11**, 447 (2017).

[20] S. Franke-Arnold, S. M. Barnett, M. J. Padgett, and L. Allen, Two-photon entanglement of orbital angular momentum states, Phys. Rev. A **65**, 033823 (2002).

[21] J. Leach, B. Jack, J. Romero, A. K. Jha, A. M. Yao, S. Franke-Arnold, D. G. Ireland, R. W. Boyd, S. M. Barnett, and M. J. Padgett, Quantum correlations in optical angle-orbital angular momentum variables, Science **329**, 662 (2010).

[22] M. J. Padgett and R. W. Boyd, An introduction to ghost imaging: Quantum and classical, Phil. Trans. R. Soc. A **375**, 20160233 (2017).

[23] L. Neves, G. Lima, J. G. Aguirre Gómez, C. H. Monken, C. Saavedra, and S. Pádua, Generation of Entangled States of Qudits using Twin Photons, Phys. Rev. Lett. **94**, 100501 (2005).

[24] A. C. Dada, J. Leach, G. S. Buller, M. J. Padgett, and E. Andersson, Experimental high-dimensional two-photon entanglement and violations of generalized Bell inequalities, Nat. Phys. **7**, 677 (2011).

[25] J. Schneeloch, C. C. Tison, M. L. Fanto, P. M. Alsing, and G. A. Howland, Quantifying entanglement in a 68-billion-dimensional quantum state space, Nat. Commun. **10**, 2785 (2019).

[26] F. Brandt, M. Hiekkamäki, F. Bouchard, M. Huber, and R. Fickler, High-dimensional quantum gates using full-field spatial modes of photons, arXiv:1907.13002 [physics, physics:quant-ph] (2019).

[27] S. J. B. Yoo, B. Guan, and R. P. Scott, Heterogeneous 2D/3D photonic integrated microsystems, Microsyst. Nanoeng. **2**, 16030 (2016).

[28] Y. Wang, V. Potoček, S. M. Barnett, and X. Feng, Programmable holographic technique for implementing unitary and nonunitary transformations, Phys. Rev. A **95**, 033827 (2017).

[29] P. Zhao, S. Li, X. Feng, S. M. Barnett, W. Zhang, K. Cui, F. Liu, and Y. Huang, Universal linear optical operations on discrete phase-coherent spatial modes with a fixed and non-cascaded setup, J. Opt. **21**, 104003 (2019).

[30] L. A. Romero and F. M. Dickey, in *Progress in Optics* (Elsevier, 2010), Vol. 54, p. 319.

[31] L. A. Romero and F. M. Dickey, Theory of optimal beam splitting by phase gratings I one-dimensional gratings, J. Opt. Soc. Am. A **24**, 2280 (2007).

[32] W. R. Clements, P. C. Humphreys, B. J. Metcalf, W. S. Kolthammer, and I. A. Walsmley, Optimal design for universal multiport interferometers, Optica **3**, 1460 (2016).

[33] H. Takesue and K. Inoue, Generation of 1.5-μm band time-bin entanglement using spontaneous fiber four-wave mixing and planar light-wave circuit interferometers, Phys. Rev. A **72**, 041804 (2005).

[34] D. F. V. James, P. G. Kwiat, W. J. Munro, and A. G. White, Measurement of qubits, Phys. Rev. A **64**, 052312 (2001).

[35] N. Bent, H. Qassim, A. A. Tahir, D. Sych, G. Leuchs, L. L. Sánchez-Soto, E. Karimi, and R. W. Boyd, Experimental Realization of Quantum Tomography of Photonic Qudits via Symmetric Informationally Complete Positive Operator-Valued Measures, Phys. Rev. X **5**, 041006 (2015).

[36] A. J. Scott and M. Grassl, Symmetric informationally complete positive-operator-valued measures: A new computer study, J. Math. Phys. **51**, 042203 (2010).

[37] D. Gross, Y.-K. Liu, S. T. Flammia, S. Becker, and J. Eisert, Quantum State Tomography via Compressed Sensing, Phys. Rev. Lett. **105**, 150401 (2010).

[38] M. A. Nielsen and I. L. Chuang, *Quantum Computation and Quantum Information* (Cambridge University Press, Cambridge, New York, 2010), 10th ed.

[39] S. M. Barnett, *Quantum Information*, Oxford Master Series in Physics. Atomic, Optical and Laser Physics No. 16 (Oxford University Press, Oxford, 2009), oCLC: ocn316430129.

[40] P. W. Shor, Polynomial-time algorithms for prime factorization and discrete logarithms on a quantum computer, SIAM Rev. **41**, 303 (1999).

[41] F. Wang, M. Erhard, A. Babazadeh, M. Malik, M. Krenn, and A. Zeilinger, Generation of the complete four-dimensional Bell basis, Optica **4**, 1462 (2017).

[42] C.-Y. Lu, D. E. Browne, T. Yang, and J.-W. Pan, Demonstration of a Compiled Version of Shor's Quantum Factoring Algorithm Using Photonic Qubits, Phys. Rev. Lett. **99**, 250504 (2007).

[43] A. Steane, Quantum computing, Rep. Prog. Phys. **61**, 117 (1998).

[44] A. Politi, J. C. F. Matthews, and J. L. O'Brien, Shor's quantum factoring algorithm on a photonic chip, Science **325**, 1221 (2009).

[45] C. H. Bennett, G. Brassard, C. Crépeau, R. Jozsa, A. Peres, and W. K. Wootters, Teleporting an Unknown Quantum State via Dual Classical and Einstein-Podolsky-Rosen Channels, Phys. Rev. Lett. **70**, 1895 (1993).

[46] N. K. Fontaine, R. Ryf, H. Chen, D. T. Neilson, K. Kim, and J. Carpenter, Laguerre-Gaussian mode sorter, Nat. Commun. **10**, 1865 (2019).

[47] M. Faraji-Dana, E. Arbabi, A. Arbabi, S. M. Kamali, H. Kwon, and A. Faraon, Compact folded metasurface spectrometer, Nat. Commun. **9**, 4196 (2018).